MJFAS
Malaysian Journal of Fundamental and Applied Sciences

RESEARCH ARTICLE

Muricins as Potential Natural B-cell Lymphoma-extra-large (Bcl-xL) Inhibitors: A Multiscale in Silico Approach Targeting Apoptosis and Chemoresistance in Cancer

Kaynat Qurban Khimani, Wan Noraini Wan Sulaiman, Noraziah Nordin*

Department of Medical Sciences I, Faculty of Medicine and Health Sciences, Universiti Sains Islam Malaysia, Persiaran Ilmu, 71800, Nilai, Negeri Sembilan, Malaysia

Abstract Resistance to apoptosis mediated by overexpression of anti-apoptotic proteins such as B-cell lymphoma-extra-large (Bcl-xL) is notable in most cancers. Natural acetogenins, including muricin I and muricin H from Annona species, are structurally unique compounds with cytotoxic potential, yet their mechanisms of action in ovarian cancer remain unexplored. This study integrates molecular docking, ADMET profiling, network pharmacology, and molecular dynamics (MD) simulations to investigate the potential of muricin I and H as Bcl-xL inhibitors. Molecular docking revealed strong binding affinities of muricin I/Bcl-xL and muricin H/Bcl-xL complexes with binding energies of –11.9 kcal/mol and –11.6 kcal/mol, respectively, suggesting potential inhibitory activity. ADMET analysis showed favourable pharmacokinetic profiles, including good oral bioavailability and low predicted toxicity (class IV). To further contextualize these findings, network pharmacology was employed to identify overlapping targets with ovarian cancer and apoptosis-related genes. Enrichment and protein–protein interaction analyses highlighted Bcl-xL and related apoptosis pathways as central nodes along with chemoresistance signalling, with key hub genes such as BCL2 and CASP3 linking to platinum resistance pathways. These findings reflect the polypharmacological nature of muricin compounds and suggest potential synergistic effects relevant to tumour progression. Finally, 100 ns of MD simulations confirmed the structural stability of muricins/Bcl-xL complexes, with consistent RMSD values of 1.29 ± 0.23 Å (muricin I) and 1.31 ± 0.16 Å (muricin H), supporting strong and stable binding interactions. This is the first study to identify muricin I and muricin H as Bcl-xL inhibitors, highlighting their potential as natural multi-target pro-apoptotic agents.

Keywords: Muricin H, Muricin I, Molecular docking, Molecular dynamics, Network pharmacology.

Introduction

Apoptosis, or programmed cell death, is tightly regulated by the Bcl-2 family of proteins, which govern the intrinsic (mitochondrial) apoptotic pathway. This family includes both pro-apoptotic members (e.g. BAX and BAK) and anti-apoptotic members (e.g. Bcl-2, Bcl-xL, Mcl-1) that form a regulatory network controlling mitochondrial outer membrane permeabilization (MOMP) through complex protein–protein interactions involving BH3 domains [1]. Activation of BAX and BAK induces oligomerization and pore formation in the mitochondrial membrane, facilitating cytochrome c release and downstream caspase activation, while anti-apoptotic proteins preserve mitochondrial integrity to inhibit apoptosis [2]. Dysregulation of Bcl-2 family proteins is implicated in many diseases, notably cancer. In fact, most malignancies rely on one or more anti-apoptotic Bcl-2 proteins for survival, making these proteins attractive drug targets [3-4]. In recent years, structure-based design has yielded small-molecule BH3 mimetics that bind the conserved hydrophobic groove of Bcl-2 family proteins [4]. ABT-737 for instance was developed via NMR screening and structure-based design to inhibit Bcl-xL, and its derivatives (navitoclax, venetoclax) demonstrated the power of rational design in targeting protein–protein interfaces [5-6]. However, development of selective Bcl-xL inhibitors has been challenging, due to on-target toxicities (e.g. thrombocytopenia). Thus, there remains a need for novel Bcl-xL inhibitors that can overcome resistance mechanisms [4].

***For correspondence:**
noraziahnordin@usim.edu.my

Received: 10 Oct. 2025
Accepted: 3 May. 2026

Bcl-xL is a key anti-apoptotic protein located at the mitochondrial outer membrane, where it binds and sequesters pro-apoptotic BH3-only proteins to inhibit MOMP. Overexpression of Bcl-xL is frequently observed in tumours and is directly linked to chemotherapy resistance [7]. Recent studies in breast cancer models show that high Bcl-xL levels correlate with poor response to chemotherapeutic agents, whereas genetic or pharmacological inhibition of Bcl-xL significantly enhances apoptosis and drug sensitivity [8]. This role of Bcl-xL in chemoresistance has motivated the search for BH3-mimetic compounds that can selectively antagonize it. Although BH3-mimetic drugs (e.g. ABT-737 and related compounds) validate this strategy, their clinical use is limited by toxicity.

Natural products with BH3-like motifs are an alternative source of inhibitors. In fact, acetogenins from the Annonaceae family (notably *Annona muricata*) have attracted attention for their anticancer activity. *Annona muricata* (soursop) is a tropical plant long known for bioactive acetogenins with potent cytotoxic effects [9]. Liaw et al. [10] first reported isolation of two new monotetrahydrofuran acetogenins, muricin H and muricin I from *A. muricata* seeds that these compounds showed significant cytotoxicity against human hepatoma cell lines (HepG2 and 2,2,15). Computational studies further support the idea that acetogenins can act as Bcl-xL inhibitors. Molecular docking and dynamics were performed in numerous *A. muricata* acetogenins against anti-apoptotic Bcl-2 proteins and found that several acetogenins bind strongly to Bcl-xL, with scores exceeding those of known inhibitors [9]. Likewise, Nordin et al. [11] used AutoDock Vina to dock a series of acetogenins and found that muricin H and I form high-affinity complexes with Bcl-xL, comparable to the reference BH3 mimetic ABT-737.

The unique structural features of muricin H and I with multiple tetrahydrofuran rings and oxygen functionalities suggest they might interact with protein targets in novel ways. Building on these insights, muricin H and muricin I emerge as compelling BH3-mimetic candidates targeting Bcl xL. To investigate their potential, cheminformatics-driven workflow was employed, comprising molecular docking and MD simulations for future optimization and experimental validation targeting Bcl xL.

Materials and Method

SwissADME physicochemical and drug-likeness profiling

The Pharmacokinetic and drug-likeness properties of muricin I and muricin H were predicted using SwissADME, a web-based platform offering rapid in silico evaluation of physicochemical parameters, pharmacokinetics, and medicinal chemistry accessibility [12]. Compound structures, encoded as SMILES strings, were submitted via the Swiss Institute of Bioinformatics server followed by the calculation of key descriptors, including Log P (lipophilicity), ESOL Log S (solubility), gastrointestinal absorption, blood–brain barrier permeability, P-glycoprotein substrate status, bioavailability, rule-of-five and other drug-likeness filters, PAINS/Brenk alerts, and synthetic accessibility.

pkCSM QSAR-based ADMET prediction

To assess metabolic fate and toxicity risks, pkCSM was used as a graph-based signature QSAR tool that predicts multiple ADMET endpoints. SMILES representations of muricin I and H were uploaded to the pkCSM web server [13]. The predictions included water solubility, Caco-2 permeability, human intestinal absorption, P-gp substrate/inhibitor status, volume of distribution (VDss), blood-brain barrier (log BB), fraction unbound in plasma, CYP substrate/inhibition profiles, total clearance, renal OCT2 substrate liability, and toxicity endpoints such as AMES mutagenicity, hERG inhibition, hepatotoxicity, LD50, and chronic toxicity (LOAEL). These parameters informed pharmacokinetic modelling and safety profiling for each compound.

PASS online mechanistic activity prediction

Predicted anticancer mechanisms were analysed using PASS Online, which applies naïve Bayesian classifiers trained on multilevel atom-neighbourhood descriptors to estimate the probability of specific biological activities (Pa) and inactivity (Pi) [14]. SMILES inputs for muricin I and H were submitted to the server. Outputs considered included antineoplastic, apoptosis agonist, antimetastatic, caspase-3 stimulant, electron transport complex I inhibitor, and TP53 expression enhancer activities. Activities with Pa greater than Pi were deemed potentially relevant and prioritised for interpretation and follow-up validation.

Functional enrichment and integrative network construction

Gene ontology (GO; BP, CC, MF) and Kyoto Encyclopaedia of Genes and Genomes (KEGG) pathway enrichment analyses were performed using DAVID v6.8 with Benjamini–Hochberg false-discovery rate (FDR) correction. Enrichment was considered significant at adjusted $p < 0.05$. This analytic framework is validated against current standards in network pharmacology. Subsequently, an integrative network was constructed in Cytoscape (v3.9.1) encompassing muricin I, muricin H, overlapping gene targets, and enriched KEGG pathways (adjusted $p < 0.05$). Compound–gene and gene–pathway interactions were represented as edges connecting nodes denoting compounds, targets, and pathways [15].

Network pharmacology analysis of muricin I and muricin H

Chemical structures of muricin I and muricin H were obtained from PubChem in canonical SMILES format. Two independent target prediction platforms were employed, including SwissTargetPrediction [16] and PharmMapper [17]. Predictions were restricted to homo sapiens targets. For consistency, only targets with a SwissTargetPrediction probability ≥ 0.60 or PharmMapper fit score ≥ 4.0 were included for subsequent analysis.

To define the disease context, gene sets related to ovarian cancer and apoptosis were retrieved. GeneCards entries with relevance score ≥ 10 and DisGeNET entries with score ≥ 0.30 were retained, generating 1,689 ovarian cancer genes and 1,320 apoptosis related genes. These were followed by an intersection analysis of drug targets and disease-associated genes. Specifically, the predicted targets of muricin I and muricin H were compared with ovarian cancer and apoptosis-related gene sets using Venny 2.1. This approach identified key overlapping targets for each compound, as well as shared targets reflecting their combined action. Such overlap analyses are commonly employed to elucidate multi-target mechanisms of drug action [18-20].

Construction and topological analysis of protein–protein interaction (PPI) network

The union of overlapping gene targets was submitted to STRING, employing a moderate confidence threshold (score ≥ 0.400) to retrieve a PPI network. The resultant network was visualised using Cytoscape v3.9.1, and the CytoHubba plugin was used to identify hub genes via degree ranking.

Target protein structure retrieval and preparation for docking

The high-resolution crystal structure of Bcl xL (PDB ID: 3ZK6) was sourced from the RCSB PDB [21]. Water molecules within 5 Å of the active site were removed using Discovery Studio Visualizer 2020 to prevent interference during docking. The Bcl-xL chain A model was modelled using SWISS-MODEL, an automated homology-modelling server that selects templates from the PDB based on sequence identity and alignment quality [22]. Missing residues were incorporated during model building, followed by energy minimisation to enhance structural accuracy. Structural integrity was confirmed via Ramachandran analysis using PROCHECK, ensuring >90% of residues occupy allowed regions. Missing hydrogens and partial charges (Kollman) were then introduced to complete the preparation of the receptor for in silico studies. The three-dimensional conformation of the target protein, providing insights into its structural features, is depicted in Figure1.

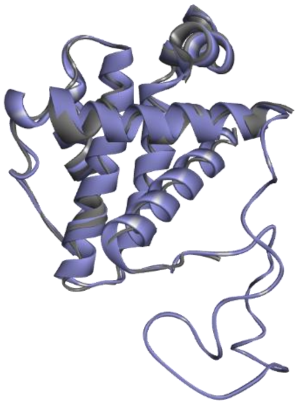

Figure 1. Three-dimensional ribbon presentation of Bcl-xL

Ligand structures preparation for docking

Two-dimensional structures of muricin H and I, as shown in Figure 2 were downloaded from PubChem and converted to PDB using Discovery Studio Visualizer. Protonation states suitable for physiological pH (7.0) were assigned, along with polar hydrogen atoms. Ligands were prepared for docking via AutoDock Tools, involving the addition of Gasteiger partial charges and conversion to PDBQT format while retaining non-polar hydrogens for proper torsion handling.

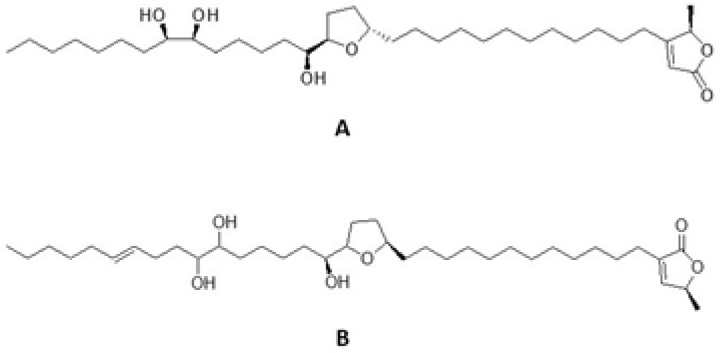

Figure 2. Ligand structures. (a) muricin H. (b) muricin I

Molecular docking simulation

Following receptor and ligand preparation, molecular docking was performed using AutoDock Vina to predict the binding modes of muricin H and I within the BH3-binding groove of Bcl xL [23]. Docking was conducted within a grid box generated using AutoGrid4, centred on the canonical BH3-binding cleft. The Lamarckian Genetic Algorithm (LGA), a hybrid global–local search method, was employed to explore conformational space and identify energetically favourable ligand orientations. Each docking run produced multiple binding poses, which were ranked by predicted binding affinity (in kcal/mol). The top-ranked conformations were subsequently analysed using to identify hydrogen bonding, hydrophobic contacts, and π–π stacking interactions. These interactions were used to characterize the binding profiles of muricin H and I within the Bcl xL active site. To ensure methodological reliability, the docking protocol was previously validated using the co-crystallized ligand of Bcl-xL, yielding an RMSD value of 0.852 Å between the redocked and native conformations. This result derived from prior in-house studies, confirms the accuracy of the docking setup in reproducing experimentally determined binding poses and supports the validity of the present docking predictions.

Molecular dynamics based structural and dynamic characterization of muricins/Bcl-xL complexes

To validate the binding poses from docking, all-atom MD simulations were conducted using AMBER 2022.1 [24]. The ff19SB force field, optimised for accurate protein backbone conformations was paired with the OPC water model, as ff19SB+OPC is recommended for high-fidelity protein simulations despite slightly increased computational cost [25]. The muricin ligands were parameterised via the general Amber force field (GAFF). Each complex was centred in an octahedral box of OPC water with an 8 Å buffer and neutralised with Na^+/Cl^- ions. Energy minimisation was performed using steepest descent and conjugate gradient methods until convergence. Equilibration involved a two-step process: initial NVT ensemble heating (0-300K) with positional restraints over 10 ns, followed by NPT (pressure= 1 atm) ensemble equilibration with gradual restraint removal. Production MD runs were conducted for 100 ns under NPT conditions at constant temperature (300K) and pressure (1 atm) with timesteps of 2 fs, employing Langevin dynamics for temperature control and isotropic scaling for pressure regulation. Long-range electrostatics were treated with the Particle Mesh Ewald (PME) method, and SHAKE constraints preserved bonds involving hydrogen atoms. Visual Molecular Dynamics (VMD) was used to visually analyse simulated trajectory data [26]. A 100 ns production trajectory was used to examine the ligands' binding capabilities. The CPPTRAJ tool was used to calculate stability metrics such as RMSD, root mean square fluctuation (RMSF), study of radius of gyration (RoG), and H-bond [27]. Graphs were generated via Xmgrace.

Results and Discussion

In silico physicochemical and drug-likeness profiling via SwissADME

The pharmacokinetic profile of muricin H and muricin I, which are two naturally occurring acetogenins, has been assessed by SwissADME and revealed some interesting properties for drug development as shown in Table 1. Firstly, the compounds have high lipophilicity with a high Log P of 8.29 and 7.70 for muricin I and muricin H, respectively. This is expected to enhance the cell membrane permeability and target engagement potential of the compounds. However, their poor aqueous solubility (ESOL Log S of −8.30 and −7.99, respectively) and low gastrointestinal absorption compromise oral bioavailability. The compounds were also non-permeant across the blood–brain barrier (BBB) and identified as P-glycoprotein (P-gp) substrates, indicating susceptibility to efflux mechanisms and further limiting systemic exposure following oral administration. Their bioavailability scores of 0.17 reflect these absorption limitations. The SwissADME bioavailability score is a composite score ranging between 0 and 1, a score lower than 0.2 is considered to be indicative of poor oral bioavailability due to a combination of low aqueous solubility, high lipophilicity, active efflux, and limited passive permeability. The observed score of 0.17, which is the same in both cases of muricins, is comparable to the score of most lipophilic natural products and indicates that formulation strategies should be implemented to address the absorption barriers before conducting in vivo tests. Importantly, neither compound inhibits major cytochrome P450 enzymes (CYP1A2, 2C9, 2C19, or 2D6), though both are predicted to undergo metabolism via CYP3A4, which could impact pharmacokinetics if co-administered with CYP3A4 modulators. Additionally, both muricin I and muricin H possess high molecular weights (>580 Da) and Log P values exceeding 4.15, thereby violating two of Lipinski's rule-of-five criteria. Despite these limitations, neither muricin I nor H triggers PAINS or Brenk alerts, reducing concerns regarding chemical reactivity or promiscuity. Furthermore, their synthetic accessibility scores (7.30 for muricin I and 7.07 for muricin H) suggest that these compounds, while moderately complex, are within range for synthesis and derivatisation.

Table 1. SwissADME-predicted physicochemical and pharmacokinetic parameters of muricin H and muricin I.

Property	Muricin H	Muricin I
Molecular weight (Da)	580.9	606.9
Consensus Log P	7.70	8.29
ESOL Log S (solubility)	−7.99	−8.30
Gastrointestinal absorption	Low	Low
BBB permeant	No	No
P-gp substrate	Yes	Yes
Bioavailability score	0.17	0.17
Lipinski violations (MW, Log P)	2	2
CYP non-inhibition (1A2,2C9,2C19,2D6)	Yes	Yes
CYP3A4 substrate	Likely	Likely
Skin permeability Log Kp	−2.79 cm/s	−2.70 cm/s
PAINS/Brenk alerts	None	None
Synthetic accessibility	7.07	7.30

Muricin I and H are found to possess encouraging properties as intracellularly targeted lead compounds, in large part because of their high lipophilicity (log P = 7.5 or more), and are thus likely to be targeted by passive diffusion across lipid-rich cell membranes. Despite the fact that high lipophilicity typically correlates with low aqueous solubility and low oral bioavailability, it can facilitate selective accumulation in intracellular compartments, including the cytoplasm or mitochondria, as has been observed with some lipophilic anticancer agents [28-29]. Notably, both muricin I and H did not cause PAINS or Brenk alerts, which corroborates the structural integrity of these scaffolds and minimizes the risks of assay interference and false-positive results in phenotypic screening. Moreover, the two compounds exhibit low predicted inhibition of major cytochrome P450 isoforms, with their metabolism being linked to CYP3A4. This profile combined with moderate synthetic accessibility scores (~7.1) are indicative that these molecules can be further optimized by existing medicinal chemistry programs.

Although their binding and specificity profiles are favourable, low aqueous solubility and low oral bioavailability are major issues. Nevertheless, these shortcomings can be mitigated with well-evaluated formulation strategies. Solid lipid nanoparticles (SLNs), nanostructured lipid carriers, and self-emulsifying drug delivery systems are examples of lipid-based drug delivery systems that have proved effective in improving the bioavailability of highly lipophilic compounds. These systems have the ability to enhance solubilization, lower efflux-based clearance, and enhance lymphatic transport of hydrophobic drugs [30-33]. Consequently, the development of muricin I and H with lipid-based delivery vehicles is a potential approach to increase systemic exposure and pharmacological efficacy. Simultaneously, rational scaffold optimization, especially the control of lipophilicity and molecular weight, can also be further used to enhance pharmacokinetic behavior without affecting biological activity. Together, these strategies offer a viable platform of progressing muricin scaffolds in silico hits to experimentally validated therapeutic candidates.

QSAR-based prediction of pharmacokinetics and toxicological liabilities

In addition to the SwissADME-based results, the pharmacokinetic and toxicity predictions obtained from the QSAR analysis were also considered for both muricin I and H to further confirm their drug-likeness and potential use for therapy (Table 2). Although both compounds have a moderate intestinal absorption potential of about 77%, they have low passive permeability according to their profiles, with Caco-2 permeability near the threshold of 0.498 – 0.501 log Papp.When determining adequate passive intestinal absorption, the Caco-2 permeability threshold is typically 0.5 log Papp or higher (10 -6 cm/s); a lower value means that absorption is probably rate-limited by passive permeability. The fact that the observed value is close to this cutoff suggests that even slight structural optimization to lower the molecular weight or lipophilicity may significantly enhance intestinal permeability and overall oral bioavailability. Additionally, both were identified as P-glycoprotein (P-gp) substrates, reinforcing concerns about efflux-limited bioavailability. Only P-gp II inhibition was predicted for both, which could influence retention in P-gp-expressing tissues. For distribution, neither compound is likely to cross the blood-brain barrier (log BB: −1.43) or penetrate the CNS (log PS: −3.089 and - 3.132). The low predicted fraction unbound and volume of distribution indicate that only a small fraction of the circulating drug (around 6% of the total) is pharmacologically active and the drug is mainly bound to plasma proteins mostly albumin or α-acid glycoprotein. The ability to bind high plasma proteins may increase half-life as the drug is not filtered by the kidneys as much; however, it also reduces the amount of free drug that is available to interact with the tumor site. This is a clinically relevant factor because compounds with high protein binding are highly likely to have a large difference in activity at different levels of plasma proteins, which change in cancer patients. In terms of metabolism, both compounds are substrates of CYP3A4, but not of CYP2D6, and they are not inhibitors of any major CYP isoforms (CYP1A2, 2C9, 2C19, 2D6, or 3A4), suggesting a low risk of metabolic drug–drug interactions. However, CYP3A4-dependent clearance implies potential variability due to polymorphism or co-administered inhibitors.

The excretion profile indicates a moderate clearance rate, and neither compound is predicted to be a substrate of the renal OCT2 transporter, suggesting hepatic metabolism as the primary elimination route. From a toxicity standpoint, both muricin I and H are non-mutagenic (AMES−), non-cardiotoxic (hERG I/II−), and non-sensitising to skin, though both demonstrate hepatotoxic potential, consistent with prior in silico predictions. The predicted hepatotoxicity is a similar concern to most natural acetogenins and lipophilic compounds, possibly due to their high Log P values that favor hepatic accumulation and CYP3A4-biomediated bioactivation to reactive intermediates. It is worth mentioning though that *in silico* hepatotoxicity models have high false-positive rates and would be necessary to experimentally validate using primary hepatic cell models or mitochondrial toxicity screens, before concluding on clinical hepatic risk. Acute and chronic oral toxicities are within the range for further toxicological characterisation of the compounds, indicated by the LD_{50} and LOAEL values. These QSAR-based profiles are in agreement with the SwissADME results and highlight the need for sophisticated formulation and optimisation strategies for the advancement of muricin derivatives.

Table 2. QSAR-derived pharmacokinetic and toxicological properties of tested muricins.

Property	Muricin H	Muricin I	Unit
Absorption			
Water Solubility	–5.313	–5.129	log mol/L
Caco-2 Permeability	0.501	0.498	log Papp (10^{-6} cm/s)
Intestinal Absorption	76.423	77.10	%
Skin Permeability	–2.732	–2.733	log Kp
P-gp Substrate	Yes	Yes	–
P-gp I / II Inhibitor	Yes/ Yes	No/ Yes	–
Distribution			
Volume of Distribution (VDss)	–0.718	–0.858	log L/kg
Fraction Unbound (Fu)	0.047	0.058	–
BBB Permeability	–1.433	–1.431	log BB
CNS Permeability	–3.132	–3.089	log PS
Metabolism			
CYP2D6 Substrate	No	No	–
CYP3A4 Substrate	Yes	Yes	–
CYP Inhibition (1A2, 2C9, 2C19, 2D6, 3A4)	No	No	–
Excretion			
Total Clearance	1.791	1.819	log mL/min/kg
Renal OCT2 Substrate	No	No	–
Toxicity			
AMES Toxicity	No	No	–
hERG I / II Inhibitor	No / No	No / No	–
Max Tolerated Dose (Human)	–0.095	–0.138	log mg/kg/day
LD_{50} (Oral Rat)	1.978	2.064	mol/kg
LOAEL (Oral Rat, Chronic)	0.244	0.249	log mg/kg_bw/day
Hepatotoxicity	Yes	Yes	–
Skin Sensitization	No	No	–
T. pyriformis Toxicity	0.294	0.289	log µg/L
Minnow Toxicity	–3.006	–3.356	log mM

Although these physicochemical and pharmacokinetic properties can serve as a valuable basis, a more detailed assessment of the therapeutic potential of muricin I and H demand a systems perspective. Here, network pharmacology provides a useful platform to explain multi-target effects and pathway-scale effects in complex disease networks like ovarian cancer. Though conventionally used with multi-component herbal formulations [34], its use with single bioactive natural compounds is gaining recognition as an effective method. It is specifically applicable considering that several small molecules introduce polypharmacological interactions with numerous protein targets that regulate numerous biological pathways [35]. Network pharmacology approach was used to describe the target landscape of muricin I and H in ovarian cancer. Target profiling demonstrated that both compounds shared a strong overlap with ovarian cancer related and apoptosis related networks. In particular, muricin I and H overlapped common targets in curated gene sets associated with ovarian cancer, and apoptotic signaling, with significant enrichment in key regulators of cell death pathways.

PASS predicted anticancer mechanisms of muricin H & muricin I

To further elucidate the therapeutic potential of muricin I and muricin H, the present study employed PASS Online, a Bayesian-based tool utilising multilevel atom-centred descriptors to predict biological activities based solely on chemical structure as shown in Table 3. Among the predicted anticancer mechanisms, both compounds showed strong antineoplastic potential, with Pa values of 0.618 for muricin I and 0.598 for muricin H, indicating a high likelihood of tumour-growth inhibition. Muricin I scored highest as an apoptosis agonist (Pa = 0.539), while muricin H showed slightly lower apoptotic potential (Pa = 0.467), consistent with programmed cell-death induction. Notably, muricin H demonstrated moderate antimetastatic activity (Pa = 0.442), whereas muricin I showed no such prediction, suggesting differential applicability. Neither compound was predicted to activate caspase 3, implying apoptosis may proceed via caspase-independent pathways. Caspase-independent apoptosis is generally associated with the mitochondria-to-nucleus translocation of apoptosis-inhibiting factor (AIF) or endonuclease G, which is activated by mitochondrial outer membrane permeabilization (MOMP). This process has been reported with a number of the annonaceous acetogenins and is compatible with the predicted activity of both muricins with the electron transport complex I inhibition activity that would induce mitochondrial dysfunction and MOMP in the absence of canonical caspase-3 executioner activity. Both also scored on electron transport complex I inhibition (Pa = 0.480 and 0.578 for muricin I and H, respectively), suggesting mitochondrial disruption and metabolic stress induction in tumour cells. Importantly, only muricin H exhibited moderate TP53 expression enhancement (Pa = 0.321), while muricin I did not (Pa = 0.134), indicating a possible preference for TP53-competent cancers versus TP53-independent contexts. Collectively, these PASS-derived predictions suggest that muricin I may modulate mitochondrial apoptosis pathways, while muricin H may function through a broader anti-cancer spectrum, including metastasis suppression and TP53 pathway engagement. These insights provide a mechanistic basis for targeted experimental validation and anticancer lead optimisation.

Table 3. PASS Online–predicted anticancer activities for muricin H and muricin I

Activity Mechanism	Muricin H	Muricin I
Antineoplastic (Tumor-growth inhibition)	0.598	0.618
Apoptosis agonist	0.467	0.539
Antimetastatic	0.442	0.000
Caspase-3 stimulant	–	–
ET Complex I inhibitor	0.578	0.480

The preliminary findings on the potential biological functionality of muricin I and muricin H against cancer-related targets were obtained using PASS Online predictions. As indicated in Table 3, the activity (Pa) of both compounds is greater than 0.5, typically a widely adopted value that shows a likely probability of biological activity in vivo [36]. These projections justify their possible usefulness as anticancer candidates, but they are to be considered as directional as opposed to conclusive. Remarkably, muricin I exhibited a relatively greater amount of the predicted activity of endpoints associated with apoptosis, indicating a reduced likelihood of triggering mitochondrial (intrinsic) apoptotic pathways. This finding is also mechanistically consistent with the postulated Bcl-xL inhibitory mode of action, i.e., the Bcl-xL-Bax/Bak blockage of interactions triggers mitochondrial outer membrane permeabilization and cytochrome c release [37]. Conversely, muricin H is more predictive of antimetastatic activity, suggesting that it may disrupt pathways that regulate epithelial-mesenchymal transition (EMT), cell adhesion, or locomotion. These effects are in line with the reported processes of structurally related acetogenins and annonaceous metabolites [38]. Interestingly, neither compound was estimated to directly activate caspase-3. This can indicate that caspase-independent apoptotic pathways are involved, which may occur via mitochondrial dysfunction or demonstrate translocation of the AIF as observed in other species of this family of compounds [39].

Integrated target–disease gene mapping and PPI network–based hub gene analysis

A total of 137 targets were predicted for muricin I and 128 targets for muricin H under stringent thresholds (probability ≥ 0.60 or fit score ≥ 4.0). These targets were intersected with curated lists of 1,689 ovarian cancer genes and 1,320 apoptosis-related genes, yielding 22 overlapping genes for muricin I, 19 for muricin H, and 11 common genes shared by both compounds (Figure 3a). Meanwhile, Figure 3(b) displays that a protein–protein interaction (PPI) network of the 30 overlapping genes using STRING (score ≥ 0.400). The network comprised 30 nodes and 82 edges while TP53, BCL2, CASP3, BAX, and TNF were identified as the top five hub proteins.

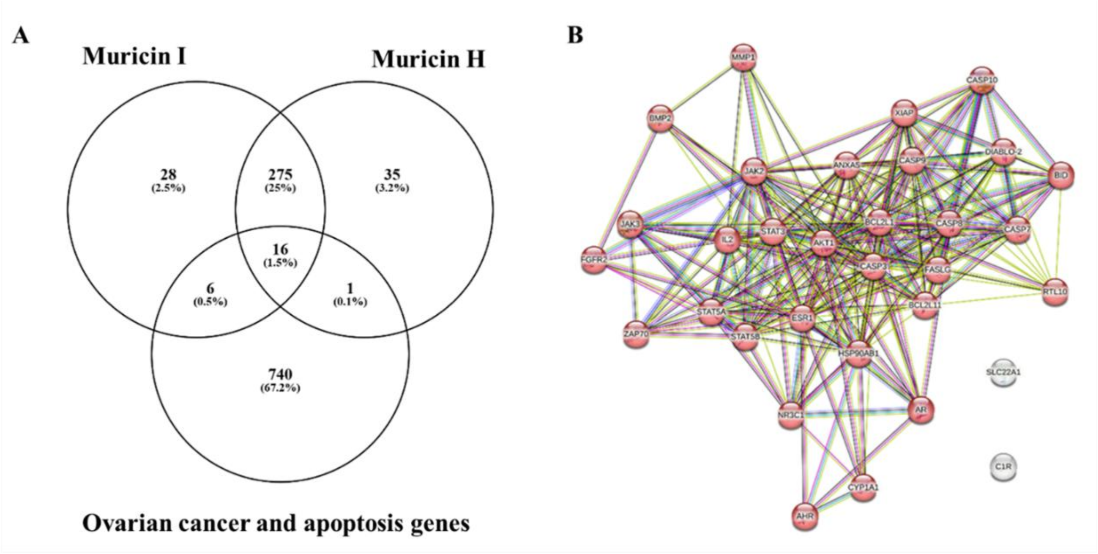

Figure 3. Overlapping targets and their interactions are explored using integrative approaches. [A] Venn diagram depicting overlapping targets among muricin I, muricin H, and ovarian cancer/apoptosis-associated genes and [B] Protein–Protein Interaction network of the overlapping targets visualized in Cytoscape; red nodes represent hub genes.

Among the top hub genes identified through protein–protein interaction network construction was BCL-2 (encoding the anti-apoptotic Bcl-xL), CASP3, TP53, BAX, and TNF. Such alignment underlines that muricins engage the intrinsic apoptosis machinery, indeed, BCL-2 family proteins are known to “play a central role in regulating apoptosis” across all apoptotic pathways, while caspase-3 is the key executioner protease in cell death. In particular, BCL-2 and its close homologue Bcl-xL inhibit apoptosis by trapping pro-apoptotic BH3-only proteins (including BAD, BIM and NOXA) as well as by inhibiting the oligomerization of BAX/BAK at the outer mitochondrial membrane. BAX/BAK-mediated cytochrome-c release is thus directly triggered by inhaling Bcl-xL and results in caspase-9 and caspase-3 activation by activating the apoptosome. The simultaneous appearance of CASP3 and BCL2 as hub nodes in the PPI network therefore mechanically connects the predicted binding activity of the muricins at Bcl-xL to the subsequent executioner caspase activation to give a consistent account of apoptotic pathway. The strong presence of BCL-2 and CASP3 in our network supports previous findings showing that BCL-2/Bcl-xL and caspase-3 expression are closely associated with platinum response in ovarian cancer [40-41]. Thus, both in silico binding data and network analysis suggest that the studied ligands can simultaneously inhibit anti-apoptotic BCL-2/Bcl-xL and activate downstream caspases, recapitulating a well-established mechanism of chemosensitisation.

Functional enrichment reveals apoptosis and platinum resistance

GO enrichment identified top pathways including apoptotic signalling, oxidative response, and mitochondrial membrane regulation. KEGG analysis highlighted five shared pathways: apoptosis, p53 signalling, PI3K-Akt, TNF, and critically platinum drug resistance. It is notable that the platinum drug resistance KEGG pathway (hsa01524) is also included in the case of ovarian cancer, where first-line platinum-based chemotherapy (carboplatin/cisplatin) often proves ineffective because of the development of resistance. This route involves several mechanisms of resistance such as increased DNA repair (ERCC1, BRCA1), augmented efflux (MRP2) and anti-apoptotic signalling through BCL-2 overexpression. Enrichment of muricin targets in this pathway suggests that muricin H and I can serve as chemosensitive with the ability to reinstate platinum sensitivity by acting on overlapping nodes and are of specific interest as combination-therapy agents in platinum-resistant ovarian cancer. These findings support a multi-target mechanism of action for muricin I and H. KEGG enrichment bar chart is illustrated in Figure 4. Detailed KEGG maps for apoptosis and platinum resistance are presented in Figure 5 and Figure 6.

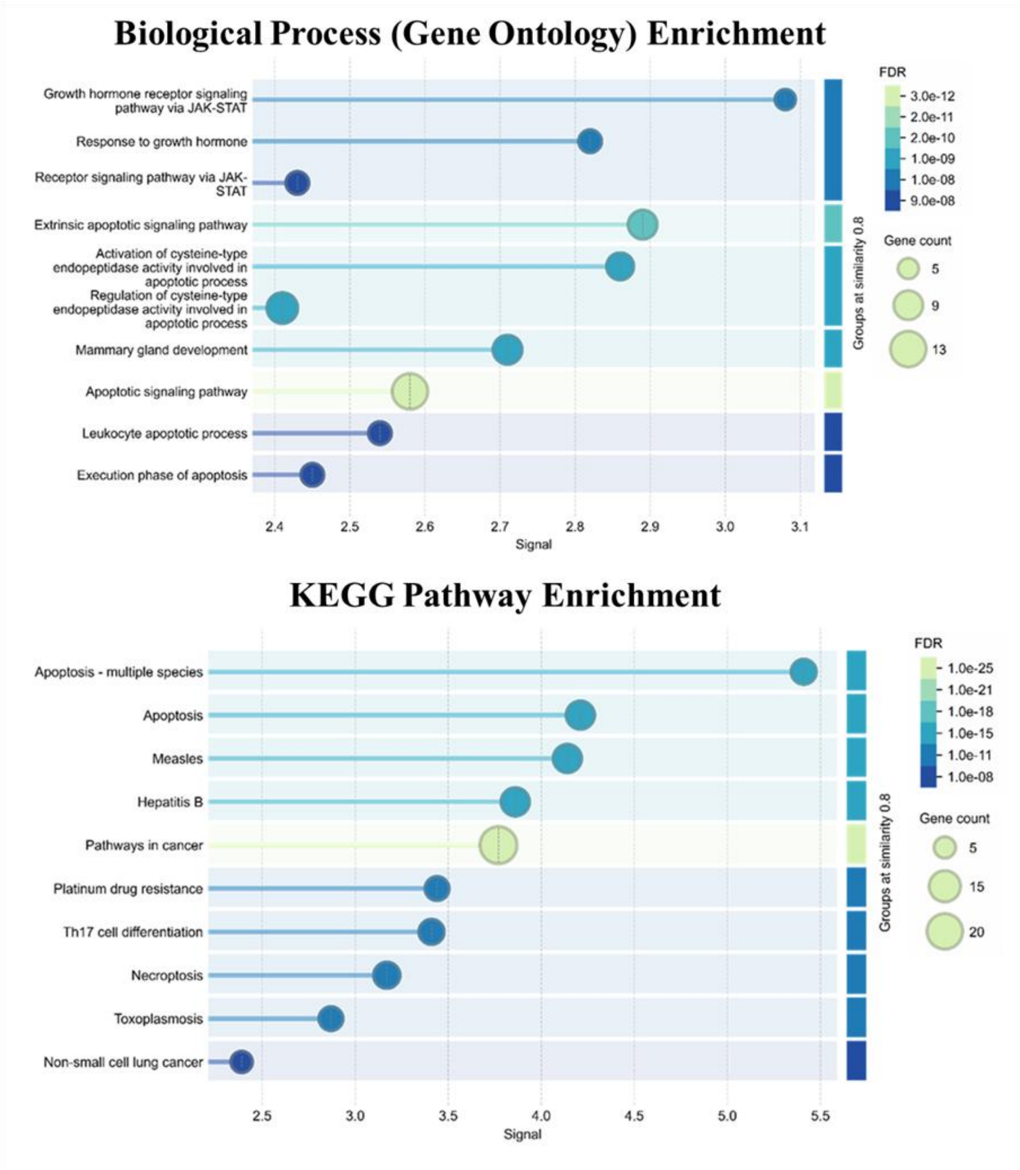

Biological Process (Gene Ontology) Enrichment

KEGG Pathway Enrichment

Figure 4. Functional enrichment analyses highlight key biological processes and pathways. [A] Bar plot showing Gene Ontology enrichment of biological processes; bar height corresponds to –$\log_{10}$ (p-value) and [B] Bar plot of the top 10 enriched KEGG pathways; bar height indicates –$\log_{10}$ (p-value).

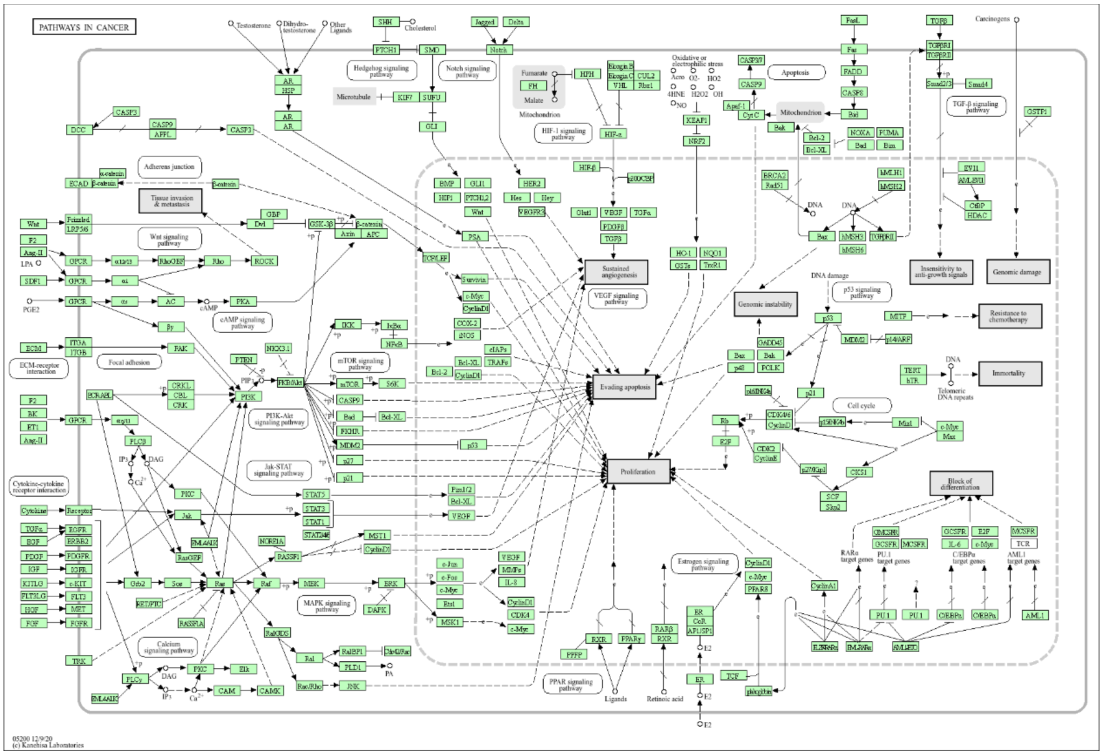

Figure 5. DAVID based KEGG pathway enrichment analysis illustrating the top pathways significantly enriched among the target gene set.

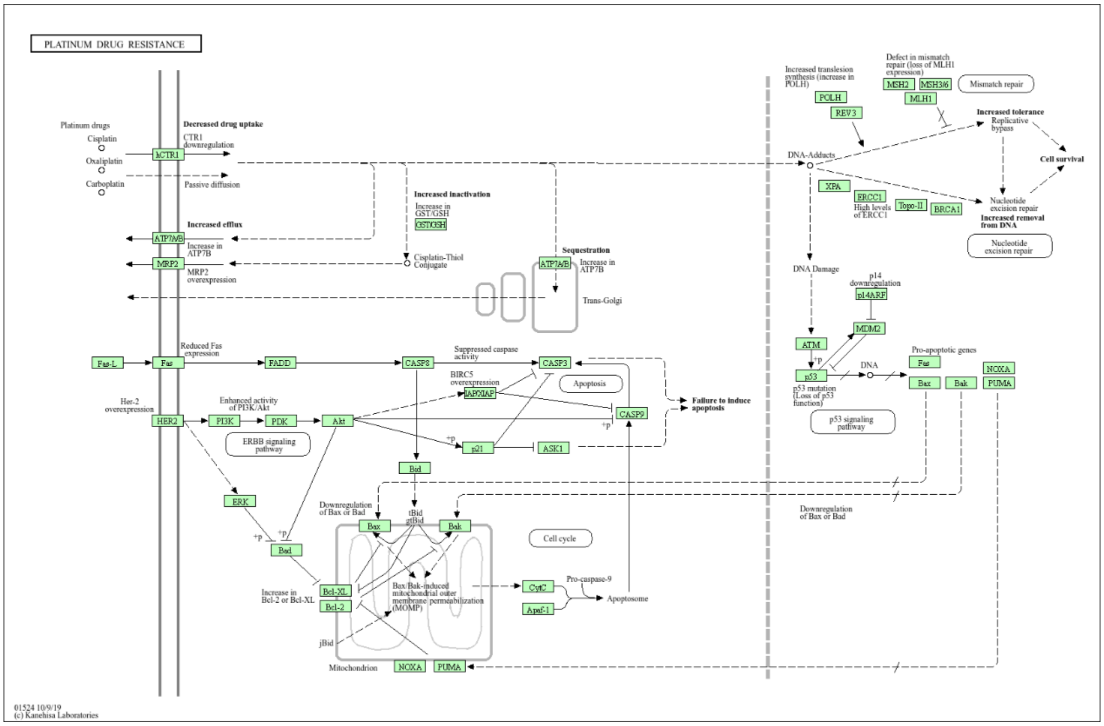

Figure 6. DAVID KEGG pathway enrichment analysis focused on platinum resistance–related targets, highlighting pathways associated with chemoresistance mechanisms.

Pathway enrichment reinforced this apoptosis-centric mechanism. Targets of both muricins were highly enriched in KEGG apoptosis, p53 signalling, PI3K-Akt, TNF and “platinum drug resistance” pathways, indicating a concerted impact on survival signalling. Platinum agents ultimately kill ovarian cells by inducing mitochondrial apoptosis, and resistance is often mediated by anti-apoptotic shifts (e.g. BCL-2 overexpression) or Akt/NF-κB survival signalling [41]. Notably, co-targeting BCL-2 with inhibitors is known to restore caspase-3/9 activation and reverse platinum resistance in ovarian models. By engaging multiple nodes (BCL-2 family, TP53/BAX pro-apoptotic axis, caspases) and upstream pathways (PI3K/Akt survival signalling, TNF/NF-κB), the muricin exhibits a multi-target mode that should lower the apoptotic threshold and counteract chemoresistance. In sum, integrated analysis predicts that muricin I/H converge on key apoptotic hubs and platinum resistance pathways, synergistically enhancing programmed cell death in ovarian cancer cells as supported by peer-reviewed mechanistic studies [41]. This systems level approach bridges molecular pharmacology with systems biology and provides a more comprehensive mechanistic framework for therapeutic exploration of individual natural compounds.

Structural insights from docking reveals key binding interactions of muricin H and muricin I with Bcl-xL

The docking results for muricin H and I against the Bcl-xL active site are summarized in Table 4 and illustrated in Figure 7 and Figure 8. Both ligands demonstrated strong docking scores with muricin H at –11.6 kcal/mol and muricin I at –11.9 kcal/mol, matching the potency range reported for other natural acetogenin Bcl-xL inhibitors (approx. –10 to –12 kcal/mol). Structurally, each ligand formed three hydrogen bonds with Bcl-xL, prominently involving the residue Arg139. In the muricin H–Bcl-xL complex, Arg139 formed two hydrogen bonds with the tetrahydrofuran moiety (2.84 Å) and its side chain (2.76 Å) as demonstrated in Figure 7. These interactions are consistent with literature characterising Arg139 as a critical hotspot in both docking and MD studies of Bcl-xL inhibitors. For muricin I, three hydrogen bonds were observed at Arg100 (2.94 Å), Arg139 (2.33 Å), and Glu129 (1.98 Å), the latter representing the shortest bond, indicative of a particularly tight interaction. As shown in Figure 7, all amino acid residues of muricin I include Phe105, Leu108, Leu130, Arg139, Val141, Ala142, Phe97, Tyr101, Tyr195 were among the identical residues that demonstrated hydrophobic interactions with muricin H and inside the Bcl-xL binding cavity.

Table 4. The interaction profile and binding affinities of muricin H and muricin I with Bcl-xL are shown in the docking data.

Ligand	Binding Affinity (kcal/mol)	Hydrogen Bonding	Hydrophobic Interaction
Muricin H	-11.6	Arg139, Arg139, Leu130	Phe105, Ala93, Arg102, Leu108 Leu130, Arg139, Val141, Ala142, Phe97, Tyr101, Phe146, Tyr195
Muricin I	-11.9	Arg139, Arg100, Glu129	Phe105, Leu108, Leu130, Arg139, Val141, Ala142, Phe97, Tyr101, Tyr195

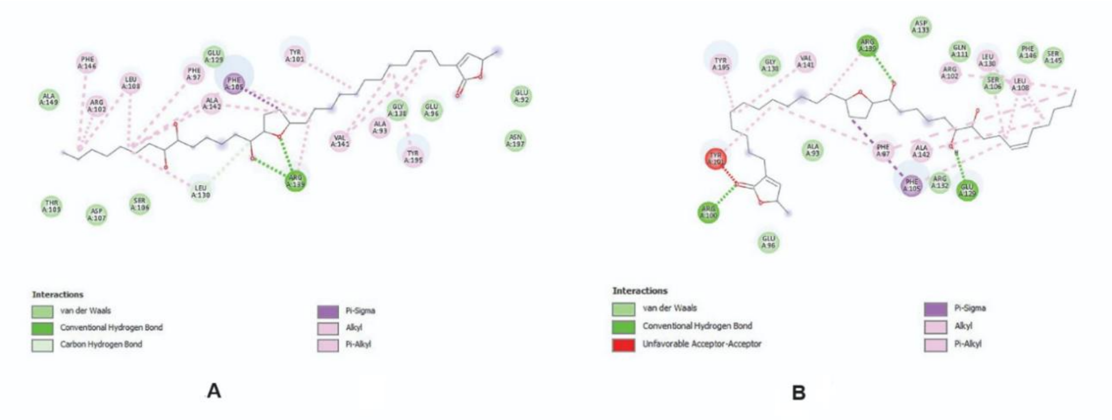

Figure 7. Illustration of the binding interaction of [A] muricin H and [B] muricin I into Bcl-xL in two dimensions. Dashed lines between ligands and protein residues show various interactions.

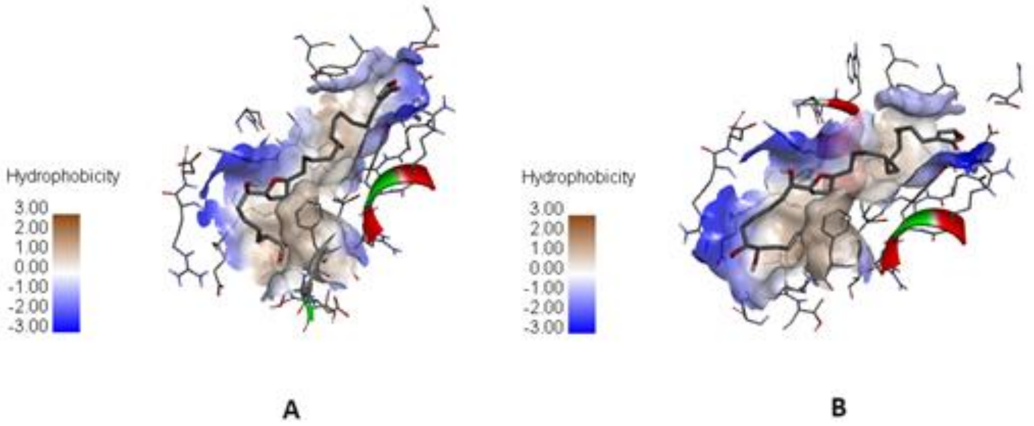

Figure 8. The hydrophobicity of the amino acid residues inside the binding cavity is revealed by the molecular interaction between A muricin H and B muricin I with the Bcl-xL binding pocket.

Both muricins H and I demonstrated stronger binding affinity for Bcl xL than the standard inhibitor ABT 737, which exhibits a binding affinity of approximately –9.2 kcal/mol [11]. A conserved interaction with Arg139, a residue pivotal for the high affinity binding of BH3 only pro apoptotic peptides, was observed for both muricins and ABT 737. Arg139 resides within the hydrophobic groove, specifically at the P2/P4 sub-pockets, where it plays a critical role in mediating inhibition. Consistent with previous docking studies of natural acetogenins, the formation of a strong conventional hydrogen bond was found with Arg139, confirming its role as a binding hotspot [42]. Other residues that occupy the binding pocket such as Glu96, Tyr101, Ser106, Asp107, Leu108, and Tyr195 are also essential in the recognition of the ligands. The subsites with the highest contribution in the binding of a ligand seems to be connected with P2 pocket, which is characterized by its depth and conformational flexibility, compared with the comparatively shallow P4 pocket [2]. P2 subpocket of Bcl-xL is bordered by Phe97, Tyr101 and Arg139 that create a deep and hydrophobic pocket that can accommodate large and flexible ligand moieties. Its conformation flexibility is due to the mobility of the α2 and 3 helices that flank the groove that can undergo induced-fit rearrangement upon the binding of a ligand. Such versatility comes as a result of the mobility of the alpha2 and alpha3 helices surrounding the binding groove that can be subjected to induced-fit changes in conformation when the ligand is bound. This structural plasticity is especially beneficial to large natural products such as muricins, with long polyketide chains, which need an open and flexible binding space. Based on this, the tighter interactions that can be seen in the P2 pocket, compared to P4, can be attributed to the stronger binding affinities of muricins over smaller synthetic ligands.

Docking analyses of muricins H and I revealed a network of stabilizing interactions within the Bcl xL binding pocket, including both hydrogen bonds and hydrophobic contacts. Hydrogen bonding, a directional and energetically significant interaction, consistently ranks among the most critical contributors to protein–ligand binding affinity [43]. Specifically, muricin H and I formed hydrogen bonds with residues such as Ser106 and Leu108, mirroring the common bonding motifs seen in potent Bcl xL inhibitors [44-45]. Moreover, there were notable hydrophobic interactions, especially with Tyr101 and Phe105, characteristic of lipophilic hot spot in P4 subsite. The hydrophobic contacts with ABT-737 are also mediated by these residues, which underscores a common binding mode between high-affinity Bcl-xL ligands [11]. In addition, these residues form the hydrophobic groove of chain A of the crystallographic Bcl-xL structure and have been shown to interact with a number of other inhibitors [46]. Lastly, the presence of residues like Arg100, and Glu129, especially Glu129 in the case of muricin I is also congruent with prior structural and molecular dynamics experiments implying the importance of the residues in ligand stabilization at the interface of BH1 and BH3 [47-48].

Dissecting structural deviations for global and core backbone stability through molecular dynamic

To evaluate the dynamic stability and conformational integrity of the muricins/Bcl-xL complexes, all-atom MD simulations of 100 ns were performed and analysed the RMSD across three domains: the full protein backbone, the core protein excluding flexible loops, and the ligands. The global RMSD profile as illustrated in Figure 9(a) revealed moderate fluctuations throughout the simulation, with muricin H exhibiting slightly higher deviations compared to muricin I, indicating the greater overall flexibility, a common outcome when simulating proteins with dynamic loop regions. Crucially, once loop regions were excluded in Figure 9(b), core backbones for both complexes stabilised featuring the average RMSD of

1.31 ± 0.16 and 1.29 ± 0.23 for muricin H and muricin I, respectively, consistent with accepted thresholds (<2 Å) for robust protein-ligand cores. Ligand RMSDs as seen in Figure 9(c) remained stable after ~25 ns, fluctuating well below the 4 Å. Throughout the 100 ns timescale, no ligand dissociation or significant pose reorientation was observed, affirming the persistence of the docking pose in line with established MD-docking validation protocols. Consequently, although global RMSD values reflect loop mobility, core region stability and persistent ligand binding provide compelling evidence of structurally sound muricin/Bcl-xL complexes, bolstering confidence in the original docking models.

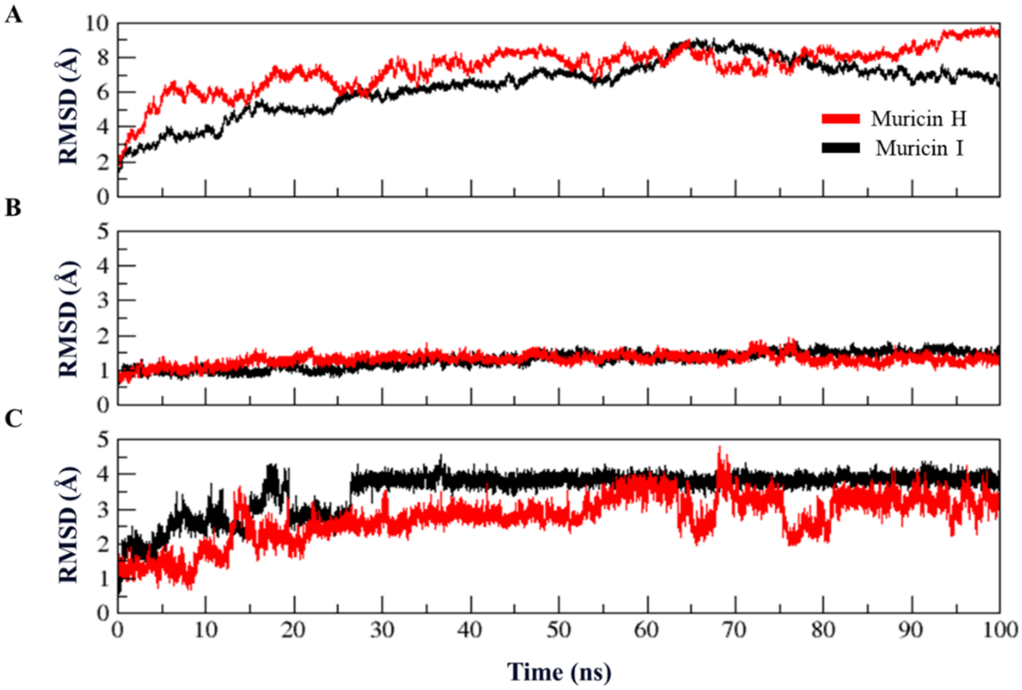

Figure 9. RMSD of Bcl-xL coupled with murucin H and muricin I in a 100 ns simulation. A RMSD for entire protein. B without loops. C RMSD of ligands

Based on these results, MD simulations revealed additional information regarding the conformational flexibility and long-term stability of the muricin I and H in the Bcl-xL protein binding pocket. As shown in Figure 9, the muricin I/Bcl-xL complex was rapidly stabilised, and after 27 ns RMSD values levelled off, indicating a stable interaction between the ligand and the protein during the 100 ns simulation [49-51]. Muricin H, however, exhibited a smooth yet progressive rise in RMSD, interrupted by oscillations, which suggests increased flexibility and dynamic movement in the binding site. The differences in the RMSD trajectories between muricin H and I might indicate different binding mechanisms, but the biological meaning of this variation remains under study. Although continued oscillations in the RMSD of muricin H are observed during the simulation, this may indicate: (i) adaptive binding conformations, (ii) inadequate convergence of the simulation, or (iii) inward flexibility in the binding pocket that does not necessarily suggest weaker binding. The small disparity in the average values of RMSF (2.95 ± 2.59 Å vs 2.73 ± 2.24 Å) is within the normal range of simulation error and is not to be interpreted without further experimental support. This local or induced flexibility may enable induced-fit interactions or allosteric modulation of Bcl-xL, which might increase its anti-apoptotic signalling inhibitory activity. Notably, the simulation demonstrated that the two ligands stayed in the binding cleft and this is indicative of their affinity and fitting into the Bcl-xL pocket, which is a characteristic required of an apoptosis-targeting anticancer agent.

Residue level fluctuations and functional motion

The RMSF analysis revealed that both muricins/Bcl xL complexes exhibit notable residue flexibility within the binding pocket as shown in Figure 10. In the muricin H complex, residues such as Glu44 and Glu45 showed elevated fluctuations (RMSF: 13.18 and 13.05 Å), indicating dynamic and variable interactions with the ligand. Similarly, the muricin I complex displayed increased RMSF at Val66 and Val67 (RMSF: 10.03 and 9.59 Å), denoting analogous mobility within the binding site. Despite these local fluctuations, the overall average RMSF for both complexes remained modest featuring the values of 2.95 ± 2.59 Å for muricin H and 2.73 ± 2.24 Å for muricin I, consistent with values reported for stable protein–ligand systems, where average RMSF typically falls between 1–3 Å, barring highly flexible loop regions. RMSF serves as a robust indicator of residue-level dynamics, with peaks identifying regions of elevated mobility while baseline RMSF reflects structural rigidity. These findings suggest that, although specific binding-pocket residues exhibit transient flexibility, the core protein–ligand interface remains structurally stable. Taken together, this dynamic profile suggests that both muricin H and I engage Bcl xL through persistent and reliable interactions, reinforcing the structural validity of their docking conformations.

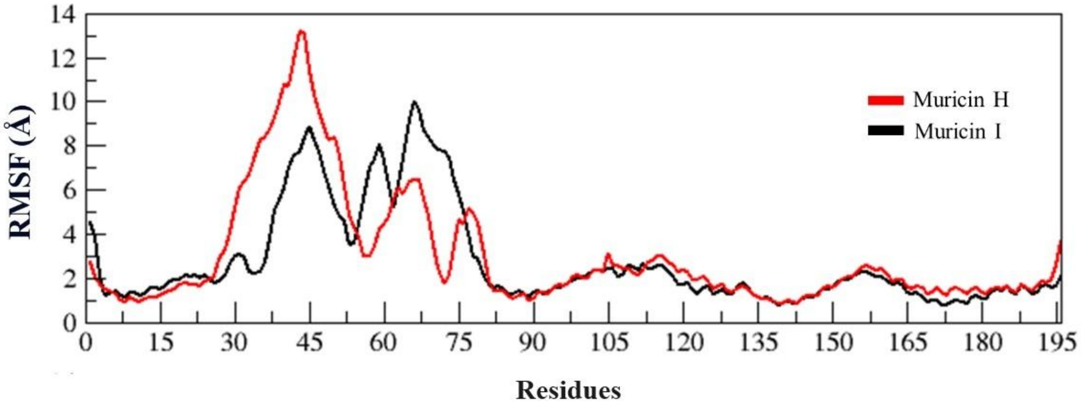

Figure 10. RMSF values for the MD simulation of the Bcl-xL protein with muricin H and muricin I.

RMSF analysis served to characterise the residue-level flexibility of Bcl-xL upon binding with muricin H and I. Distinct fluctuations were observed in specific regions of the protein–ligand complexes, suggesting that ligand-induced conformational changes may influence the anti-apoptotic activity of Bcl-xL. Notably, elevated RMSF values often indicate enhanced local flexibility due to structural adaptation around the ligand, whereas lower values are associated with stable domains such as the canonical hydrophobic groove responsible for sequestering pro-apoptotic BH3-only proteins [52]. Localized increases in RMSF observed for both muricin H and I may thus reflect an induced flexibility that facilitates displacement of native Bcl-xL ligands, ultimately favouring pro-apoptotic signalling.

Insights into structural integrity across the simulation

The radius of gyration (RoG) is an important parameter that defines the distribution of atoms around the center of mass. In addition, it acts as an indicator of the compactness of the protein structure. Lower and constant RoG values indicate the maintenance of a well-folded and structurally stable conformation over time [53, 54]. In the present study, the muricin I/Bcl-xL complex showed a slightly lower mean RoG compared to the muricin H. This indicates the enhanced compactness of the structure and the stabilization of the interface.

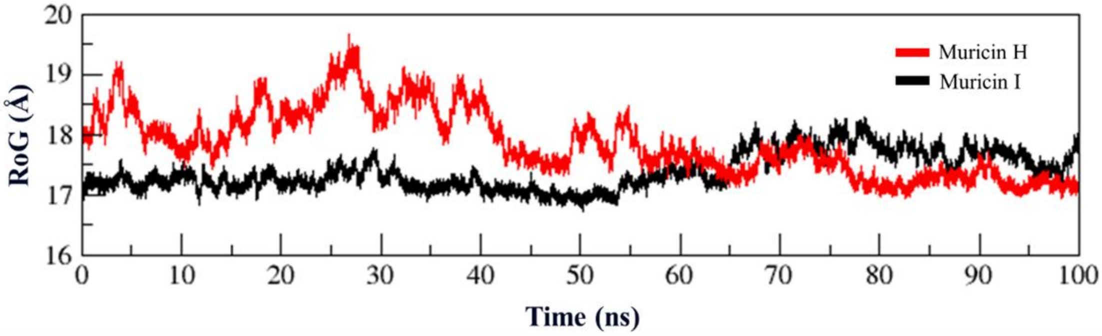

Figure 11. Analyzing the radius of gyration (RoG) in the molecular dynamics (MD) simulation trajectory of muricin H and muricin I with the Bcl-xL protein over a 100 ns time interval.

In line with this observation, the muricin H/Bcl-xL and muricin I/Bcl-xL complexes were in comparatively similar state of structural compactness during the entire 100 ns simulation, with a mean RoG of 17.86 ± 0.55 and 17.39 ± 0.31 respectively. The RoG profiles of both systems were strongly plateauing, which is typical of stable protein-ligand complexes. Changes within the range of 0.5A are mostly accepted and regarded to be a sign of conformational stability. Thus, the low degree of variation in both simulations implies that neither of the muricin ligands triggers notable unfolding or abnormal compaction of Bcl-xL, which supports the structural integrity of the complexes and strengthens their validity as stable docking models. This reduced RoG of the muricin I/Bcl-xL complex could be due to conformational changes at the Bcl-xL binding groove, especially the rearrangements of the α-helices forming the BH3-binding site. The BH3-binding groove is surrounded in Bcl-xL by helical 5 residues (alpha1, 2, 3, and 5) mainly. A decrease in RoG and constant RMSD (as seen in the case of muricin I) is associated with a compaction of these helices around the ligand, effectively reducing the width of the groove and enhancing van der Waals and hydrophobic complementarity. Interactions with BH3 peptides or ligands typically induce an opening of the hydrophobic groove where α3 shifts away from the peptide and in most cases becomes less helical and disordered, though to different degrees depending on the peptide, while the α4 helix moves towards the peptide, and overall, the groove becomes more open and V-shaped. Conformational rearrangement with backbone mobility and side chain rearrangement of residues located specifically in helices 2, 3, and 5 can be caused by small molecule binding. This form of induced conformational rearrangement involving major backbone refolding and helical segment motions in the binding site have been found in other high-affinity Bcl-xL inhibitors, and this sort of interaction has been linked to be more selective and stable in binding the site [55-57]. On the other hand, muricin H triggered a relatively mild effect on RoG, indicating a more flexible or loosely packed structure. These changes in structural dynamics are supported by previous studies showing that the ligand has the potential to influence the tertiary structure of Bcl-xL, which may trigger a pro-apoptotic effect [58].

Post-dynamic interaction

Following the completion of the 100 ns MD trajectory, a thorough post-simulation analysis of intermolecular contacts was conducted to assess the stability and persistence of ligand–protein interactions, critical for validating docking accuracy. Interaction profiling revealed that residues Arg139, Leu130, Phe105, Tyr101, and Tyr195 consistently participate in hydrogen bond formation as illustrated in Figure 12. These contacts were not transient but persisted throughout the simulation, indicating strong anchoring of muricin H within the Bcl-xL binding groove. A similar network of stabilizing interactions was observed, with Arg139, Glu129, Leu108, Tyr101, and Tyr195 forming durable hydrogen bonds over the course of the MD simulation. Notably, Tyr101 and Tyr195 are common to both complexes, highlighting them as conserved "hot-spot" residues pivotal to ligand binding. These observations underscore the reliability of the predicted docking conformations and the formation of stable, functionally relevant interactions under dynamic physiological conditions.

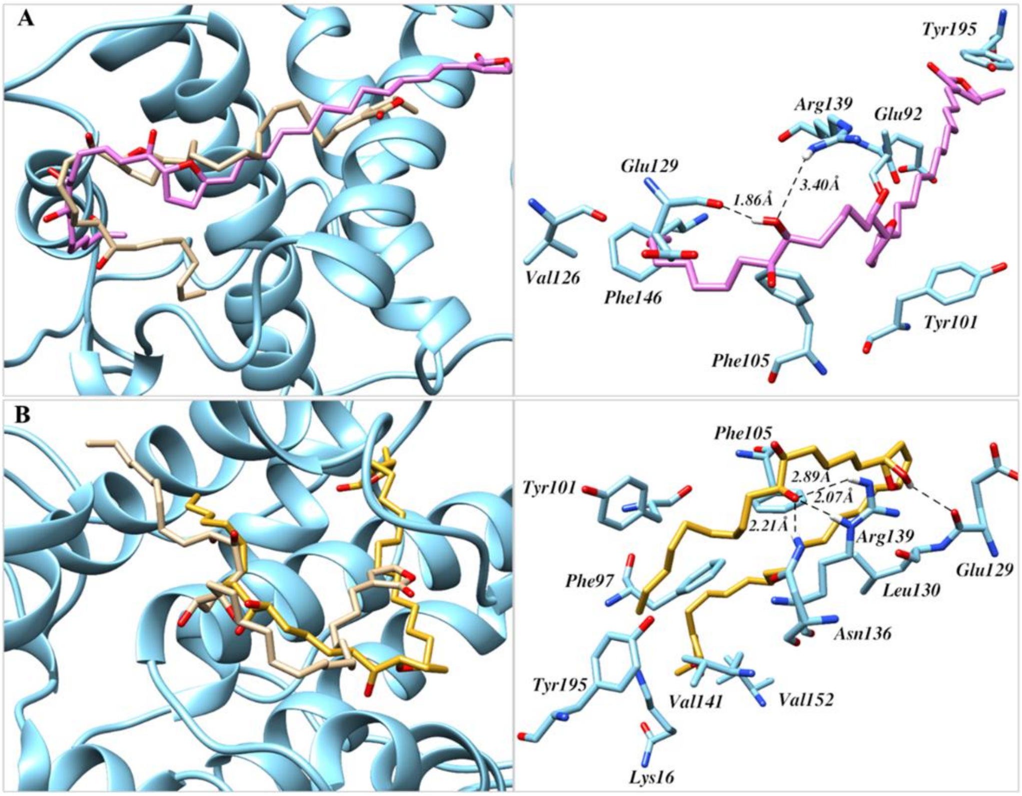

Figure 12. An illustration of the interactions between the ligands and Bcl-xL complex from simulated trajectories. [A] muricin H and [B] muricin I. The overlap of initial structures (stick model) and their binding configurations are shown on the diagram's left side. The accompanying right-side panel displays a more thorough view.

Further insight into binding stability was obtained through dynamic hydrogen bonding and hydrophobic interaction analyses. While docking simulations primarily revealed hydrophobic contacts, MD trajectories uncovered additional time-dependent hydrogen bonds, suggesting the presence of transient stabilising interactions. Dynamic or transiently formed H-bonds Time-dependent hydrogen bonds, also known as dynamic or time-dependent H-bonds, are hydrogen bonds that form and break over nanosecond timescales due to thermal fluctuations in the protein and ligand. In contrast to the challenges of static docking, MD trajectories record occupancy of these bonds throughout the entire simulation window; bonds with occupancy at least 30 percent are typically viewed as pharmacologically important contributors to binding free energy. The presence of these bonds in both muricin complexes (Figure 12) not predicted by docking indicates that the actual binding affinity can be lower than that determined by the docking scores alone, further supporting the argument that these compounds are true Bcl-xL inhibitors. Despite their structural similarity, muricin H and I displayed differential residue-level binding preferences within the Bcl-xL pocket. These differences underscore the importance of subtle scaffold features in dictating interaction specificity and protein conformational response, which are critical for rational inhibitor optimisation.

Conclusions

This study shows that both muricin I and H are able to form stable and structurally coherent complexes with the anti-apoptotic protein Bcl-xL in a long-term MD simulation. It is interesting to note that the rapid stabilisation of muricin I was a consequence of tight and consistent interaction whereas greater flexibility in RMSD was observed in muricin H, which indicates that an induced-fit mechanism could be involved and thereby improves the inhibitory activity. The observed dynamic profiles are in agreement with other similar phytochemical-Bcl-xL complexes, in which conformational plasticity between ligand-protein interactions is associated with ability to induce apoptosis. RMSF and RoG studies have shown that muricin I induce structural compaction and rigidity in the Bcl-xL hydrophobic binding groove, but that muricin H permits more localised flexibility. These behaviours are consistent with results of recent natural-product BCL-2 family inhibitors, in which analogous dynamic changes mediated anti-apoptotic function interference. Moreover, hydrogen bonding and hydrophobic contacts mapping using MD shows stable interactions across the two ligands, which serve as a molecular explanation of selective binding. Taken together, these results make muricin I and H strong Bcl-xL-inhibitory candidates. Their unique dynamic interplay of stable interaction to adaptive flexibility provides the structural strategies to the explicit design of the next generation of inhibitors that can induce robust apoptotic activities. These insights provide a good basis of the further development of muricin-based scaffolds into therapeutic development. Quantitative binding-affinity measurements (MM/PBSA), experimental structural validation and functional assays should be the future aims of the research to support these encouraging computational predictions.

Conflicts of Interest

The authors declare that there is no conflict of interest regarding the publication of this paper.

Acknowledgment

We would like to thank Universiti Sains Islam Malaysia for providing the funding for this research under the PPP grant (PPPI/FPSK/0121/USIM/16421). We would like to express our gratitude to Michele Cosi from University of Arizona for his guidance and technical support of the simulation software.

References

[1] Saddam, M., Paul, S. K., Habib, M. A., Fahim, M. A., Mimi, A., Islam, S., Paul, B., & Helal, M. M. U. (2024). Emerging biomarkers and potential therapeutics of the BCL-2 protein family: The apoptotic and anti-apoptotic context. Egyptian Journal of Medical Human Genetics, 25(1), 12. https://doi.org/10.1186/s43042-024-00485-7

[2] Czabotar, P. E., Lessene, G., Strasser, A., & Adams, J. M. (2014). Control of apoptosis by the BCL-2 protein family: Implications for physiology and therapy. Nature Reviews Molecular Cell Biology, 15(1), 49–63. https://doi.org/10.1038/nrm3722

[3] Man, K. F., Darweesh, O., Hong, J., Thompson, A., O'Connor, C., Bonaldo, C., Melkonyan, M. N., Sun, M., Patel, R., Ellisen, L. W., & Robinson, T. (2025). CREB1–BCL2 drives mitochondrial resilience in RAS GAP-dependent breast cancer chemoresistance. Oncogene, 44(16), 1093–1105. https://doi.org/10.1038/s41388-025-03284-5

[4] Vogler, M., Braun, Y., Smith, V. M., Westhoff, M. A., Pereira, R. S., Pieper, N. M., Anders, M., Callens, M., Vervliet, T., Abbas, M., & Macip, S. (2025). The BCL2 family: From apoptosis mechanisms to new advances in targeted therapy. Signal Transduction and Targeted Therapy, 10(1), 91. https://doi.org/10.1038/s41392-025-02176-0

[5] Souers, A. J., Leverson, J. D., Boghaert, E. R., Ackler, S. L., Catron, N. D., Chen, J., Dayton, B. D., Ding, H., Enschede, S. H., Fairbrother, W. J., & Huang, D. C. (2013). ABT-199, a potent and selective BCL-2 inhibitor, achieves antitumor activity while sparing platelets. Nature Medicine, 19(2), 202–208. https://doi.org/10.1038/nm.3048

[6] Birkinshaw, R. W., Gong, J. N., Luo, C. S., Lio, D., White, C. A., Anderson, M. A., Blombery, P., Lessene, G., Majewski, I. J., Thijssen, R., & Roberts, A. W. (2019). Structures of BCL-2 in complex with venetoclax reveal the molecular basis of resistance mutations. Nature Communications, 10(1), 2385. https://doi.org/10.1038/s41467-019-10363-1

[7] Stevens, M., & Oltean, S. (2019). Modulation of the apoptosis gene Bcl-x function through alternative splicing. Frontiers in Genetics, 10, 804. https://doi.org/10.3389/fgene.2019.00804

[8] Nocquet, L., Roul, J., Lefebvre, C. C., Duarte, L., Campone, M., Juin, P. P., & Souazé, F. (2024). Low BCL-xL expression in triple-negative breast cancer cells favors chemotherapy efficacy, and this effect is limited by cancer-associated fibroblasts. Scientific Reports, 14(1), 14177. https://doi.org/10.1038/s41598-024-64696-z

[9] Antony, P., & Vijayan, R. (2016). Acetogenins from Annona muricata as potential inhibitors of antiapoptotic proteins: A molecular modeling study. Drug Design, Development and Therapy, 10, 1399–1410. https://doi.org/10.2147/DDDT.S103216

[10] Liaw, C. C., Chang, F. R., Lin, C. Y., Chou, C. J., Chiu, H. F., Wu, M. J., & Wu, Y. C. (2002). New cytotoxic monotetrahydrofuran Annonaceous acetogenins from Annona muricata. Journal of Natural Products, 65(4), 470–475. https://doi.org/10.1021/np0105578

[11] Nordin, N., Khimani, K., & Abd Ghani, M. F. (2021). Acetogenins exhibit potential BCL-XL inhibitor for the induction of apoptosis in the molecular docking study. Current Drug Discovery Technologies, 18(6), 98–108. https://doi.org/10.2174/1570163818666210204202426

[12] Daina, A., Michielin, O., & Zoete, V. (2019). SwissTargetPrediction: Updated data and new features for efficient prediction of protein targets of small molecules. Nucleic Acids Research, 47(W1), W357–W364. https://doi.org/10.1093/nar/gkz382

[13] Pires, D. E., Blundell, T. L., & Ascher, D. B. (2015). pkCSM: Predicting small-molecule pharmacokinetic and toxicity properties using graph-based signatures. Journal of Medicinal Chemistry, 58(9), 4066–4072. https://doi.org/10.1021/acs.jmedchem.5b00104

[14] Filimonov, D. A., Lagunin, A. A., Gloriozova, T. A., Rudik, A. V., Druzhilovskii, D. S., Pogodin, P. V., & Poroikov, V. V. (2014). Prediction of the biological activity spectra of organic compounds using the PASS online web resource. Chemistry of Heterocyclic Compounds, 50(3), 444–457. https://doi.org/10.1007/s10593-014-1496-1

[15] Dong, Z., Chang, X., Luo, X., Li, H., Deng, M., Huang, Z., Chen, T., Chen, Y., Sun, B., Wu, Y., & Wu, R. (2025). Integration of network pharmacology, transcriptomics, and experimental verification to investigate the mechanism of action of cepharanthine hydrochloride against prostate cancer. Scientific Reports, 15(1), 18115. https://doi.org/10.1038/s41598-025-03004-9

[16] Daina, A., Michielin, O., & Zoete, V. (2019). SwissTargetPrediction: Updated data and new features for efficient prediction of protein targets of small molecules. Nucleic Acids Research, 47(W1), W357–W364. https://doi.org/10.1093/nar/gkz382

[17] Liu, X., Ouyang, S., Yu, B., Liu, Y., Huang, K., Gong, J., Zheng, S., Li, Z., Li, H., & Jiang, H. (2010). PharmMapper server: A web server for potential drug target identification using pharmacophore mapping approach. Nucleic Acids Research, 38(Suppl_2), W609–W614. https://doi.org/10.1093/nar/gkq300

[18] Chen, J., Li, L. F., Hu, X. R., Wei, F., & Ma, S. (2021). Network pharmacology-based strategy for elucidating the molecular basis for the pharmacologic effects of licorice (Glycyrrhiza spp.). Frontiers in Pharmacology, 12, 590477. https://doi.org/10.3389/fphar.2021.590477

[19] Wang, J., Wang, Y., Li, L., Cai, S., Mao, D., Lou, H., & Zhao, J. (2023). Network pharmacology-based pharmacological mechanism prediction of Lycii Fructus against postmenopausal osteoporosis. Medicine, 102(48), e36292. https://doi.org/10.1097/MD.0000000000036292

[20] Jain, N. K., Tailang, M., Chandrasekaran, B., Khazaleh, N. T., Thangavel, N., Makeen, H. A., Albratty, M., Najmi, A., Alhazmi, H. A., Zoghebi, K., & Alagusundaram, M. (2024). Integrating network pharmacology with molecular docking to rationalize the ethnomedicinal use of Alchornea laxiflora (Benth.) Pax & K. Hoffm. for efficient treatment of depression. Frontiers in Pharmacology, 15, 1290398. https://doi.org/10.3389/fphar.2024.1290398

[21] Lessene, G., Czabotar, P. E., Sleebs, B. E., Zobel, K., Lowes, K. N., Adams, J. M., Baell, J. B., Colman, P. M., Deshayes, K., Fairbrother, W. J., & Flygare, J. A. (2013). Structure-guided design of a selective BCL-XL inhibitor. Nature Chemical Biology, 9(6), 390–397. https://doi.org/10.1038/nchembio.1246

[22] Waterhouse, A., Bertoni, M., Bienert, S., Studer, G., Tauriello, G., Gumienny, R., Heer, F. T., de Beer, T. A. P., Rempfer, C., Bordoli, L., & Lepore, R. (2018). SWISS-MODEL: Homology modelling of protein structures and complexes. Nucleic Acids Research, 46(W1), W296–W303. https://doi.org/10.1093/nar/gky427

[23] Trott, O., & Olson, A. J. (2010). AutoDock Vina: Improving the speed and accuracy of docking with a new scoring function, efficient optimization, and multithreading. Journal of Computational Chemistry, 31(2), 455–461. https://doi.org/10.1002/jcc.21334

[24] Lee, T. S., Cerutti, D. S., Mermelstein, D., Lin, C., LeGrand, S., Giese, T. J., Roitberg, A., Case, D. A., Walker, R. C., & York, D. M. (2018). GPU-accelerated molecular dynamics and free energy methods in Amber18: Performance enhancements and new features. Journal of Chemical Information and Modeling, 58(10), 2043–2050. https://doi.org/10.1021/acs.jcim.8b00462

[25] Hao, X., Li, C., Liu, C., Meng, Q., & Sun, J. (2022). The performance of OPC water model in prediction of the phase equilibria of methane hydrate. Journal of Chemical Physics, 157(1), Article 014101. https://doi.org/10.1063/5.0093659

[26] Humphrey, W., Dalke, A., & Schulten, K. (1996). VMD: Visual molecular dynamics. Journal of Molecular Graphics, 14(1), 33–38. https://doi.org/10.1016/0263-7855(96)00018-5

[27] Roe, D. R., & Cheatham, T. E. III. (2013). PTRAJ and CPPTRAJ: Software for processing and analysis of molecular dynamics trajectory data. Journal of Chemical Theory and Computation, 9(7), 3084–3095. https://doi.org/10.1021/ct400341p

[28] Jeliński, T., Przybyłek, M., & Cysewski, P. (2019). Natural deep eutectic solvents as agents for improving solubility, stability and delivery of curcumin. Pharmaceutical Research, 36(8), 116. https://doi.org/10.1007/s11095-019-2643-2

[29] Gangavarapu, A., Tapia-Lopez, L. V., Sarkar, B., Pena-Zacarias, J., Badruddoza, A. Z. M., & Nurunnabi, M. (2024). Lipid nanoparticles for enhancing oral bioavailability. Nanoscale, 16(39), 18319–18338. https://doi.org/10.1039/D4NR01487A

[30] Elnady, R. E., Amin, M. M., & Zakaria, M. Y. (2023). A review on lipid-based nanocarriers mimicking chylomicron and their potential in drug delivery and targeting infectious and cancerous diseases. AAPS Open, 9(1), 13. https://doi.org/10.1186/s41120-023-00080-x

[31] Sambhakar, S., Saharan, R., Narwal, S., Malik, R., Gahlot, V., Khalid, A., Najmi, A., Zoghebi, K., Halawi, M. A., Albratty, M., & Mohan, S. (2023). Exploring lipids for their potential to improve bioavailability of lipophilic drug candidates: A review. Saudi Pharmaceutical Journal, 31(12), 101870. https://doi.org/10.1016/j.jsps.2023.101870

[32] Seo, Y., Lim, H., Park, H., Yu, J., An, J., Yoo, H. Y., & Lee, T. (2023). Recent progress of lipid nanoparticles-based lipophilic drug delivery: Focus on surface modifications. Pharmaceutics, 15(3), 772. https://doi.org/10.3390/pharmaceutics15030772

[33] Uti, D. E., Alum, E. U., Atangwho, I. J., Ugwu, O. P. C., Egbung, G. E., & Aja, P. M. (2025). Lipid-based nano-carriers for the delivery of anti-obesity natural compounds: Advances in targeted delivery and precision therapeutics. Journal of Nanobiotechnology, 23(1), 336. https://doi.org/10.1186/s12951-025-03412-z

[34] Shao, L. I., & Zhang, B. (2013). Traditional Chinese medicine network pharmacology: Theory, methodology and application. Chinese Journal of Natural Medicines, 11(2), 110–120. https://doi.org/10.1016/S1875-5364(13)60037-0

[35] Li, H., Zhao, L., Zhang, B., Jiang, Y., Wang, X., Guo, Y., Liu, H., Li, S., & Tong, X. (2014). A network pharmacology approach to determine active compounds and action mechanisms of Ge-gen-qin-lian decoction for treatment of type 2 diabetes. Evidence-Based Complementary and Alternative Medicine, 2014, 495840. https://doi.org/10.1155/2014/495840

[36] Lagunin, A., Stepanchikova, A., Filimonov, D., & Poroikov, V. (2000). PASS: Prediction of activity spectra for biologically active substances. Bioinformatics, 16(8), 747–748. https://doi.org/10.1093/bioinformatics/16.8.747

[37] Youle, R. J., & Strasser, A. (2008). The BCL-2 protein family: Opposing activities that mediate cell death. Nature Reviews Molecular Cell Biology, 9(1), 47–59. https://doi.org/10.1038/nrm2308

[38] Bermejo, A., Figadère, B., Zafra-Polo, M. C., Barrachina, I., Estornell, E., & Cortes, D. (2005). Acetogenins from Annonaceae: Recent progress in isolation, synthesis and mechanisms of action. Natural Product Reports, 22(2), 269–303. https://doi.org/10.1039/B500186M

[39] Mollinedo, F., & Gajate, C. (2020). Lipid rafts as signaling hubs in cancer cell survival/death and invasion: Implications in tumor progression and therapy. Journal of Lipid Research, 61(5), 611–635. https://doi.org/10.1194/jlr.TR119000439

[40] Gregoraszczuk, E. L., Rak-Mardyła, A., Ryś, J., Jakubowicz, J., & Urbański, K. (2015). Effect of chemotherapeutic drugs on caspase-3 activity as a key biomarker for apoptosis in ovarian tumor cells cultured as monolayer: A pilot study. Iranian Journal of Pharmaceutical Research, 14(4), 1153–1161.

[41] Yuan, J., Lan, H., Jiang, X., Zeng, D., & Xiao, S. (2020). Bcl-2 family: Novel insight into individualized therapy for ovarian cancer. International Journal of Molecular Medicine, 46(4), 1255–1265. https://doi.org/10.3892/ijmm.2020.4689

[42] Boyenle, I. D., Ogunlana, A. T., Oyedele, A. Q. K., Olokodana, B. K., Owolabi, N., Salahudeen, A., Aderenle, O. T., Oloyede, T. O., & Adelusi, T. I. (2023). Reinstating apoptosis using putative Bcl-xL natural product inhibitors: Molecular docking and ADMETox profiling investigations. Journal of Taibah University Medical Sciences, 18(3), 461–469. https://doi.org/10.1016/j.jtumed.2022.10.014

[43] Grinevicius, V. M., Andrade, K. S., Mota, N. S., Bretanha, L. C., Felipe, K. B., Ferreira, S. R., & Pedrosa, R. C. (2019). CDK2 and Bcl-xL inhibitory mechanisms by docking simulations and anti-tumor activity from piperine-enriched supercritical extract. Food and Chemical Toxicology, 132, 110644. https://doi.org/10.1016/j.fct.2019.110644

[44] Abd Ghani, M. F., Othman, R., & Nordin, N. (2020). Molecular docking study of naturally derived flavonoids with antiapoptotic BCL-2 and BCL-XL proteins toward ovarian cancer treatment. Journal of Pharmacy and Bioallied Sciences, 12(Suppl 2), S676–S680. https://doi.org/10.4103/jpbs.JPBS_272_19

[45] Bekker, G. J., Araki, M., Oshima, K., Okuno, Y., & Kamiya, N. (2023). Mutual induced-fit mechanism drives binding between intrinsically disordered Bim and cryptic binding site of Bcl-xL. Communications Biology, 6(1), 349. https://doi.org/10.1038/s42003-023-04720-6

[46] Fulda, S., & Kroemer, G. (2011). Mitochondria as therapeutic targets for the treatment of malignant disease. Antioxidants & Redox Signaling, 15(12), 2937–2949. https://doi.org/10.1089/ars.2011.4078

[47] Arsianti, A., Fadilah, L. E., & Paramita, R. I. (2017). Molecular docking of antimycin A. Asian Journal of Pharmaceutical and Clinical Research, 10(8), 317–322. https://doi.org/10.22159/ajpcr.2017.v10i8.18165

[48] Nordin, N., Sulaiman, W. N. W., & Elias, M. H. (2024). Molecular docking of natural alkaloids with Bcl-xL protein in the apoptosis process. Malaysian Journal of Science, Health & Technology, 10(2), 139–146. https://doi.org/10.33102/mjosht.v10i2.406

[49] Umar, A. K., Zothantluanga, J. H., Luckanagul, J. A., Limpikirati, P., & Sriwidodo, S. (2023). Structure-based computational screening of 470 natural quercetin derivatives for identification of SARS-CoV-2 Mpro inhibitor. PeerJ, 11, e14915. https://doi.org/10.7717/peerj.14915

[50] Pandya, V., Rao, P., Prajapati, J., Rawal, R. M., & Goswami, D. (2024). Pinpointing top inhibitors for GSK3β from pool of indirubin derivatives using rigorous computational workflow and their validation using molecular dynamics simulations. Scientific Reports, 14(1), 49. https://doi.org/10.1038/s41598-023-50992-7

[51] Rana, N., Solanki, P., Mehra, R., & Manhas, A. (2025). Identification of natural compound inhibitors for substrate-binding site of MTHFD2 enzyme: Insights from structure-based drug design and biomolecular simulations. Chemical Physics Impact, 10, 100809. https://doi.org/10.1016/j.chphi.2024.100809

[52] Krishna, S., Kumar, S. B., Murthy, T. K., & Murahari, M. (2021). Structure-based design approach of potential BCL-2 inhibitors for cancer chemotherapy. Computers in Biology and Medicine, 134, 104455. https://doi.org/10.1016/j.compbiomed.2021.104455

[53] Abouzied, A. S., Alqarni, S., Younes, K. M., Alanazi, S. M., Alrsheed, D. M., Alhathal, R. K., Huwaimel, B., & Elkashlan, A. M. (2024). Structural and free energy landscape analysis for the discovery of antiviral compounds targeting the cap-binding domain of influenza polymerase PB2. Scientific Reports, 14(1), 25441. https://doi.org/10.1038/s41598-024-69816-3

[54] Lobanov, M. Y., Bogatyreva, N. S., & Galzitskaya, O. V. (2008). Radius of gyration as an indicator of protein structure compactness. Molecular Biology, 42(4), 623–628. https://doi.org/10.1134/S0026893308040195

[55] Lama, D., Modi, V., & Sankararamakrishnan, R. (2013). Behavior of solvent-exposed hydrophobic groove in the anti-apoptotic Bcl-XL protein: clues for its ability to bind diverse BH3 ligands from MD simulations. PLoS One, *8*(2), e54397. https://doi.org/10.1371/journal.pone.0054397

[56] Parikh, N., Koshy, C., Dhayabaran, V., Perumalsamy, L. R., Sowdhamini, R., & Sarin, A. (2007). The N-

terminus and alpha-5, alpha-6 helices of the pro-apoptotic protein Bax, modulate functional interactions with the anti-apoptotic protein Bcl-xL. BMC cell biology, *8*(1), 16. https://doi.org/10.1186/1471-2121-8-16

[57] Leber, B., Lin, J., & Andrews, D. W. (2010). Still embedded together binding to membranes regulates Bcl-2 protein interactions. Oncogene, 29(38), 5221-5230. https://doi.org/10.1038/onc.2010.283

[58] Wakui, N., Yoshino, R., Yasuo, N., Ohue, M., & Sekijima, M. (2018). Exploring the selectivity of inhibitor complexes with Bcl-2 and Bcl-xL: A molecular dynamics simulation approach. Journal of Molecular Graphics and Modelling, 79, 166–174.